Extended source models for wind turbine noise propagation

B. Cotté[1, a)]

Institute of Mechanical Sciences and Industrial Applications (IMSIA),

ENSTA ParisTech, CNRS, CEA, EDF, Université Paris-Saclay

828 bd des Maréchaux, 91120 Palaiseau, France

(Dated: 31 January 2019)

Accurate prediction of wind turbine noise propagation over long distances requires to model the dominant broadband aerodynamic noise sources, as well as the main outdoor sound propagation effects. In this study, two methods are compared to include extended aeroacoustic source models in a parabolic equation code for wind turbine noise propagation in an inhomogeneous atmosphere. In the first method, an initial starter is obtained for each segment of the blade using the backpropagation approach. In the second method, the blade segments are viewed as moving monopole sources, and only a limited number of parabolic equation simulations are needed for different source heights across the rotor plane. The two methods are compared to the point source approximation first in a homogeneous medium for validation purposes, and then in a stratified inhomogeneous atmosphere. The results show that an extended source model is necessary to calculate the sound pressure level upwind, where a shadow zone is present, and to obtain the correct amplitude modulation levels. Furthermore, the second method is seen to yield as accurate results as the first method when a sufficient number of source heights is considered, with a computation time that is much reduced.

[a)] benjamin.cotte@ensta-paristech.fr

I. INTRODUCTION

Wind turbine noise can be perceived at distances greater than one kilometer and is characterized by amplitude modulations at the receiver (Larsson and Öhlund, 2014; Zajamsek *et al.*, 2016). As noise restrictions limit the areas where onshore wind farms can be built, an accurate prediction of the far-field noise is needed in order to improve the placement of the turbines at a given site, as well as to develop noise mitigation methods. This requires to model the dominant broadband aerodynamic noise sources as well as the main outdoor sound propagation effects that occur between the wind turbines and the receivers. The main aerodynamic noise sources are generally considered to be turbulent inflow noise, corresponding to the interaction of atmospheric turbulence with the blade leading edge, and trailing edge noise, corresponding to the scattering of the turbulent boundary layer at the blade trailing edge. As shown in the experimental campaign of Buck *et al.* (2016), turbulent inflow noise is generally dominant at low frequencies, typically below 300-400 Hz for a modern upwind turbine, while trailing edge noise dominates at higher frequencies, as already shown by Oerlemans and Schepers (2009).

To model aerodynamic noise sources, the state-of-the-art approach is to divide the wind turbine blades into radial segments, and to sum incoherently the noise contributions from each segment at the receiver locations (Oerlemans and Schepers, 2009; Zhu *et al.*, 2005). To model atmospheric propagation, however, this approach is rarely used, and it is more common to model the wind turbine as a point source of specified power located at the rotor center (Lee *et al.*, 2016; Prospathopoulos and Voutsinas, 2007). Recently, several methods

have been proposed to include an extended source model in wind turbine noise propagation calculations. McBride and Burdisso (2017) and Heimann *et al.* (2018) have considered extended models in ray-based models. McBride and Burdisso (2017) have kept all the blade segments used in the aeroacoustic source model in their 3D ray-tracing approach, while Heimann *et al.* (2018) consider 24 fixed point sources distributed over the rotor disk with an identical sound power level (no source model used). One of the known weaknesses of these ray-based models is the treatment of diffraction, for instance in the presence of an acoustic shadow zone. Other authors have proposed methods based on the parabolic equation (PE), that is able to treat diffraction effects accurately. Barlas *et al.* (2017) have considered a PE model considering only one point source per blade. This point source is located at the segment location where the maximum noise level is calculated by their aerodynamic noise source model for each frequency. Cotté (2018) has kept several segments along the blade, and has used the backpropagation method to preserve the directivity of the noise sources, which makes the approach very computationally demanding.

In this study, two methods are compared to include extended aeroacoustic source models in a parabolic equation code for acoustic propagation in an inhomogeneous atmosphere. The source model is based on Amiet's theory (Roger and Moreau, 2010; Tian and Cotté, 2016), but the methods could be applied to other source models, such as the so-called BPM semi-empirical model that is widely used in wind turbine noise prediction studies (Oerlemans and Schepers, 2009; Zhu *et al.*, 2005). In the first method, that was recently proposed (Cotté, 2018), an initial starter for the PE model is obtained for each segment of the blade using the backpropagation approach. In the second method, that is introduced in the present study,

the blade segments are viewed as moving monopole sources, and only a limited number of parabolic equation simulations are needed which strongly reduces the computation time. The two methods are compared to the point source approximation, first in a homogeneous medium for validation purposes and second in a stratified atmosphere.

The paper is organized as follows. In Section II, the source and propagation models are described, as well as the proposed extended source methods. Then, the models are compared in Section III, first in a homogeneous atmosphere to be validated against an analytical solution, and then in an inhomogeneous atmosphere to take into account refraction effects in different directions of propagation.

II. DESCRIPTION OF THE EXTENDED SOURCE MODELS

A. Description of the broadband noise sources using strip theory

It is common in the literature to calculate the noise spectrum of a full blade using strip theory (Christophe *et al.*, 2009; Rozenberg *et al.*, 2010; Sinayoko *et al.*, 2013). This theory consists in dividing the blade into M small segments or strips along the radial direction in order to take into account the variation of the blade geometry and the incident flow, as schematically shown in Fig. 1(a). Each segment is represented as an airfoil of chord c_m and span L_m, $m = 1, .., M$. The different segments are supposed to be uncorrelated, so that the noise contributions from all blade segments can be summed at the receiver. This assumption is one of the main limitation of strip theory at low frequencies, as discussed by Christophe *et al.* (2009).

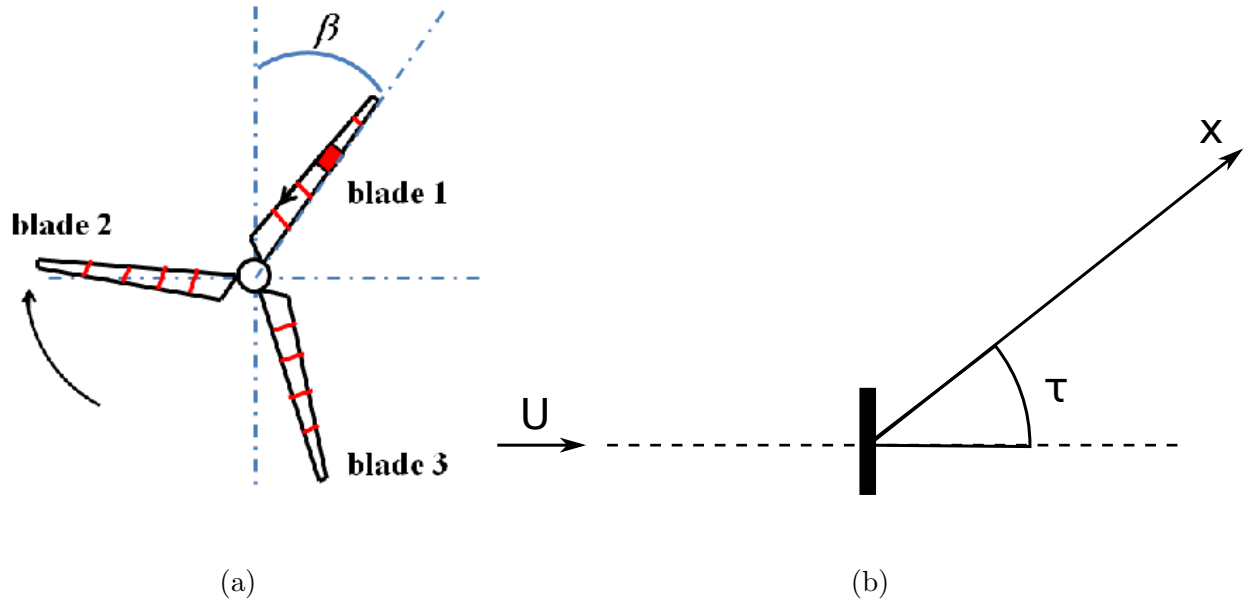

(a) (b)

FIG. 1. Notations for (a) the rotor plane with blades divided into segments, and (b) the wind turbine propagation in a direction τ with respect to the direction of the wind U.

For each segment at each angular position β, the power spectral density (PSD) of the acoustic pressure p for the rotating airfoil at angular frequency ω is written (Sinayoko *et al.*, 2013; Tian and Cotté, 2016):

$$S_{pp}^{R}(\mathbf{x_R^T}, \omega, \beta) = \frac{\omega_e}{\omega} S_{pp}^{F}(\mathbf{x_R^B}, \omega_e, \beta), \tag{1}$$

with ω_e the emission angular frequency, $\mathbf{x_R^T}$ the receiver coordinates in the wind turbine reference system, $\mathbf{x_R^B}$ the receiver coordinates in the blade reference system, and S_{pp}^{F} the PSD for an airfoil that is fixed relative to the receiver. The expression for the Doppler factor ω/ω_e is given in Sinayoko *et al.* (2013).

In order to calculate the PSD of acoustic pressure S_{pp}^{F} for an airfoil that is fixed relative to the receiver, various methods have been proposed in the literature. In this study, a model of trailing edge noise and turbulent inflow noise for wind turbines based on Amiet's theory

is used, that is detailed in Tian and Cotté (2016). The model is valid for an aspect ratio $L_m/c_m \geq 3,\ m = 1..M$, and the receiver is supposed to be in the far-field.

B. Acoustic propagation model based on the parabolic approximation

The acoustic propagation model considered here is a parabolic equation with fractional steps, called split-step Padé, based on higher order Padé approximants and solved with the method of Collins (1993). It has been shown in Cotté (2018) for a typical wind turbine configuration that it is more computationally effective than a classical wide-angle parabolic equation based on a Padé (1,1) approximation of the propagation operator. In this study, the effective sound speed approximation is used, which allows one to take into account the refraction effects due to the vertical wind gradients in the equation for a medium at rest:

$$c_{\text{eff}}(z) = c(z) + U(z)\cos\tau = \sqrt{\gamma_0 r T(z)} + U(z)\cos\tau, \tag{2}$$

with z the height above ground, γ_0 the specific-heat ratio, r the specific gas constant, $U(z)$ and $T(z)$ the mean vertical profiles of wind speed and temperature, and τ the angle between the wind direction and the propagation direction from the source to the receiver noted as x, as shown in Fig. 1(b). In order to introduce the notations needed for the extended source models described in Secs. II C and II D, the main equations of the model are briefly reminded below.

Using the axisymmetric approximation, the three-dimensional Helmholtz equation can be reduced to the following two-dimensional equation in the far-field:

$$\left[\frac{\partial^2}{\partial x^2} + \left(\frac{\partial}{\partial z^2} + k^2\right)\right] q_c = 0, \tag{3}$$

where $q_c = p_c\sqrt{x}$ connects the q_c variable to the complex pressure p_c, and k is the acoustic wavenumber. This wavenumber can be written as $k^2 = k_0^2 n^2 = k_0^2(1+\epsilon)$, where $n(z) = c_0/c_{\text{eff}}(z)$ is the index of refraction and $k_0 = \omega/c_0$ is the value of the acoustic wavenumber at the reference sound speed c_0. Introducing the propagation operator

$$\mathcal{Q} = \left(1 + \epsilon + \frac{1}{k_0^2}\frac{\partial}{\partial z^2}\right)^{1/2} = (1+\mathcal{L})^{1/2}, \tag{4}$$

that is independent of x in range-independent media, Eq. (5) becomes (Gilbert and White, 1989):

$$\left(\frac{\partial}{\partial x} + ik_0\mathcal{Q}\right)\left(\frac{\partial}{\partial x} - ik_0\mathcal{Q}\right) q_c = 0. \tag{5}$$

We can decouple Eq. (5) into two equations characterizing a wave propagating in the positive x direction, denoted as q_+ (propagating wave), and a wave propagating in the negative x direction denoted as q_- (backpropagating wave). Using the notation $\gamma = \pm 1$, one obtains from Eq. (5):

$$\left(\frac{\partial}{\partial x} - \mathrm{i}\gamma k_0\mathcal{Q}\right) q_\gamma = 0. \tag{6}$$

Introducing the variable ϕ_γ corresponding to the envelope of the pressure:

$$q_\gamma(x,z) = \phi_\gamma(x,z)\exp(\mathrm{i}\gamma k_0 x), \tag{7}$$

and substituting Eq. (7) into Eq. (6), the following equation is obtained:

$$\frac{\partial \phi_\gamma}{\partial x} = \mathrm{i}\gamma k_0\left(\mathcal{Q}-1\right)\phi_\gamma. \tag{8}$$

To solve Eq. (8), the domain is discretized using a rectangular mesh of size Δx and Δz along the x and z-axis respectively. The split-step Padé (N,N) method is used to advance the field from x to $x+\Delta x$ for $\gamma = 1$, or from x to $x-\Delta x$ for $\gamma = -1$ (Collins, 1993; Dallois

123 *et al.*, 2002).The angular validity increases with the order N of the development and depends
124 on the mesh size Δx chosen (Dallois *et al.*, 2002). As shown in Cotté (2018), accurate results
125 are obtained in a typical wind turbine configuration with N = 2 and mesh sizes $\Delta x = 2\lambda$ and
126 $\Delta z = \lambda/10$, where λ is the acoustic wavelength. Along the vertical direction, the domain is
127 bounded by a ground impedance condition at $z = 0$, and by an absorbing layer at the top
128 of the domain to obtain non-reflecting boundary conditions (Salomons, 2001).

129 C. Extended source model based on the backpropagation method (Amiet-PE 130 model)

131 The first extended source model considered in this study is based on the parabolic equa-
132 tion property to decouple forward and backward-propagating waves, as shown in Eqs. (6)
133 and (8). It was proposed by Cotté (2018) and is called Amiet-PE model. The basics of the
134 method are summarized in this section.

135 For each segment m, each angular position β of the blade and each angular frequency
136 ω, a parabolic equation calculation is performed for which an initial condition at $x = 0$ is
137 needed. This initial condition is obtained numerically using the backpropagation method,
138 whose principle is illustrated in Fig. 2(a). It consists first in back-propagating a known
139 pressure field, that is noted "initial solution" in Fig. 2(a), at $x = x_{is}$ to $x = 0$, taking
140 $\gamma = -1$ in the equations. Then, in a second step, the starter at $x = 0$ is forward-propagated
141 to the desired distance using the "classical" parabolic equation with $\gamma = +1$.

142 In the backpropagation method, the initial solution at $x = x_{is}$ is obtained for heights
143 $z_{is,p} = p\Delta z, p = 0..P$, from the expression (1) for the PSD of acoustic pressure of a rotating

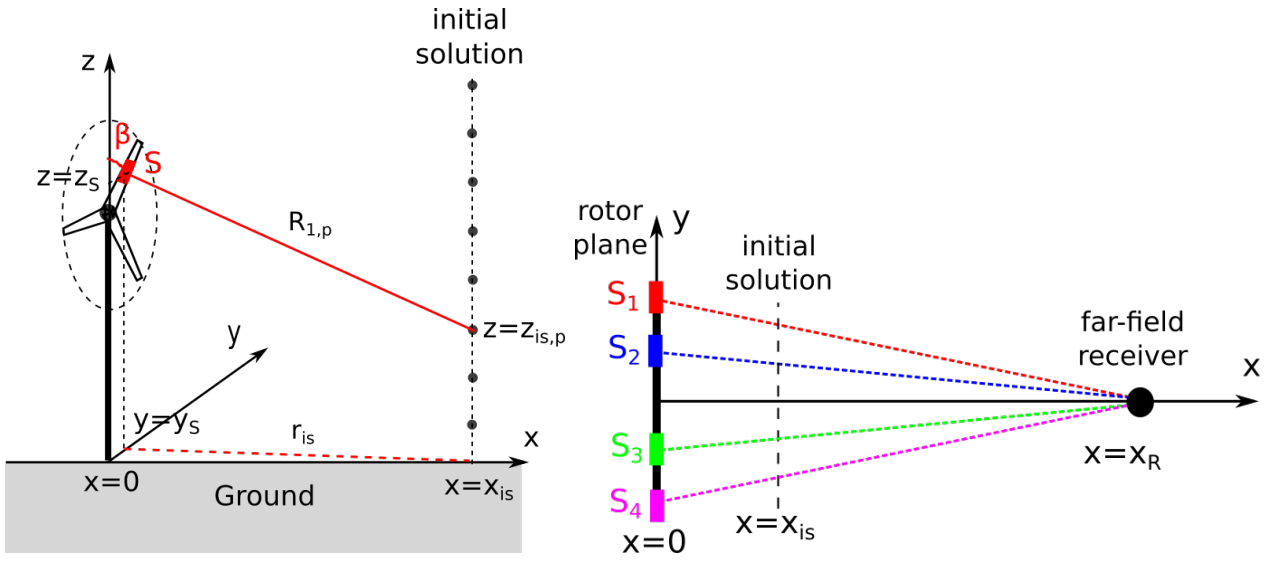

(a) (b)

FIG. 2. Schematics for (a) the backpropagation method used to obtain the starter at $x = 0$ from the initial solution at $x = x_{is}$ for one blade segment S, and (b) the different propagation planes between 4 blade segments noted S_1, S_2, S_3 and S_4 and the far-field receiver at $x = x_R$ (top view). Color online.

blade. The initial solution thus includes the source directivity as viewed by this vertical line of receivers in this specific direction. In the presence of ground, the initial solution is written:

$$q_c(z_{is,p}) = \sqrt{S^R_{pp}(\mathbf{x_R^T}, \omega, \beta)}\sqrt{x_S}\mathrm{e}^{\mathrm{i}k_0 R_{1,p}} \times \left(1 + Q\frac{R_{1,p}}{R_{2,p}}\mathrm{e}^{\mathrm{i}k_0(R_{2,p}-R_{1,p})}\right), \tag{9}$$

where $R_{1,p} = \sqrt{r_{is}^2 + (z_S - z_{is,p})^2}$ and $R_{2,p} = \sqrt{r_{is}^2 + (z_S + z_{is,p})^2}$ are respectively the distance between the segment at $(0, y_S, z_S)$ or the image segment at $(0, y_S, -z_S)$ and the p^{th} initial starter point, with $r_{is} = \sqrt{x_{is}^2 + (y_S - y_{is})^2}$, and Q is the spherical wave reflection coefficient.

During the backpropagation calculation, the atmosphere is supposed homogeneous and the ground is taken as rigid ($Q = 1$). Then, the starter at $x = 0$ can be propagated using any ground impedance and any sound speed profile. Note also that each calculation is performed in a slightly different plane that crosses the far-field receiver at $x = x_R$, as shown in Fig. 2(b). This method is therefore strictly exact only at this distance. For $x \neq x_R$, the total acoustic pressure is obtained by summing contributions with different y values. Since the radius of the rotor (typically 50 m) is generally small compared to the propagation distances considered, the method remains valid over a wide range of distances. The computational cost of this method is quite high, since MN_β PE calculations per frequency and per propagation direction need to be performed, where N_β is the number of angular positions used to discretize the rotor plane.

D. Extended source model based on moving monopoles (MM model)

The second extended source model considered in this study represents each segment of the blade as a monopole rotating at angular velocity $\dot{\beta}$. It is called the moving monopoles (MM) model. Compared to the first method, it does not rely on the parabolic approximation and can be applied to any propagation model.

In the MM model, the sound pressure level (SPL) at the receiver is calculated for a segment m at angular position β using the point source approximation (Salomons, 2001):

$$\begin{aligned} \mathrm{SPL}(\omega, \beta) = \mathrm{SWL}(\omega, \beta) - 10\log_{10}(4\pi R_1^2) \\ + \Delta L(\omega, \beta) - \alpha(\omega) R_1, \end{aligned} \tag{10}$$

where $\mathrm{SWL}(\omega,\beta)$ is the angle-dependent sound power level (SWL), $R_1=\sqrt{x^2+y_S^2+(z_S-z)^2}$ is the distance between the segment at $(0,y_S,z_S)$ and the receiver at $(x,0,z)$, ΔL is the sound pressure relative to the free field, and α is the absorption coefficient in dB/m.

The angle-dependent SWL can be obtained from the free-field SPL calculated using Amiet's model. Assuming free-field conditions ($\Delta L=0$) and no absorption in the medium, Eq. (10) becomes:

$$\begin{aligned}\mathrm{SWL}(\omega,\beta)&=\mathrm{SPL}_{FF}(\omega,\beta)+10\log_{10}(4\pi R_1^2)\\&=10\log_{10}\left(\frac{S_{pp}^R(\mathbf{x_R^T},\omega,\beta)}{p_{\mathrm{ref}}^2}\right)+10\log_{10}(4\pi R_1^2),\end{aligned}\tag{11}$$

with SPL_{FF} the free-field SPL and $p_{\mathrm{ref}}=20\,\mu$Pa the reference pressure. From Eqs. (10) and (11), the following equation for $\mathrm{SPL}(\omega,\beta)$ is obtained:

$$\begin{aligned}\mathrm{SPL}(\omega,\beta)=10\log_{10}&\left(\frac{S_{pp}^R(\mathbf{x_R^T},\omega,\beta)}{p_{\mathrm{ref}}^2}\right)\\&+\Delta L(\omega,\beta)-\alpha(\omega)R_1.\end{aligned}\tag{12}$$

In Eq. (12), the main unknown is the relative sound pressure level $\Delta L(\omega,\beta)$. For the propagation over a finite impedance ground in a homogeneous atmosphere at rest, it can be calculated analytically (Salomons, 2001):

$$\Delta L=10\log_{10}\left|1+Q\frac{R_1}{R_2}\mathrm{e}^{\mathrm{i}k_0(R_2-R_1)}\right|^2,\tag{13}$$

with $R_2=\sqrt{x^2+y_S^2+(z_S+z)^2}$ the distance between the image-source and the receiver.

In order to include refraction effects, $\Delta L(\omega,\beta)$ can be calculated using the parabolic approximation method described in Sec. II B. The initial starter corresponding to the monopole source is calculated numerically using the backpropagation method in order to preserve the angular validity of the split-step Padé (2,2) method (Galindo, 1996). In order to limit the

number of PE calculations to perform, a set of N_h source heights distributed along the rotor plane are considered:

$$H_n = H_{\min} + n\Delta H, \quad n = 0, .., N_h - 1, \tag{14}$$

with ΔH the height step given by:

$$\Delta H = \frac{H_{\max} - H_{\min}}{N_h - 1}, \tag{15}$$

where $H_{\min}$ and $H_{\max}$ are respectively the minimum and maximum heights to consider. The relative sound pressure level $\Delta L(\omega, \beta)$ in Eq. (12) is then obtained using a nearest-neighbor interpolation. As an example, the monopole sources are represented for the three blades in Fig. 3 with $M = 6$ segments per blade. Using $N_h = 5$ source heights in the MM model, the sources are shifted to a fictive position determined by the nearest-neighbor interpolation, as shown by the arrows in Fig. 3. The maximum difference between the fictive and exact source heights is thus $\Delta H/2$. Note that these fictive positions are only used to calculate $\Delta L(\omega, \beta)$ in Eq. (10), since the variables $\mathrm{SWL}(\omega, \beta)$ and R_1 are calculated from the exact source positions.

As a result, there are N_h PE calculations to perform per frequency and per propagation direction in the MM model. The computational cost of MM model is thus reduced compared to the Amiet-PE model since $N_h < MN_\beta$ in practice. On the other hand, the MM model does not consider the source directivity in the vertical direction.

Note finally that the point source approximation is a special case of the MM model, where only one PE calculation is performed for a source located at the hub height. It is still possible in this case to obtain the evolution of the SPL with respect to the angular position

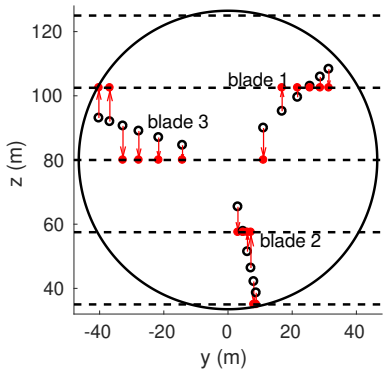

FIG. 3. Exact (○) and fictive (●) positions of the monopole sources distributed along each blade in the MM model at $\beta = 48^o$ with $M = 6$ segments and $N_h = 5$ source heights represented as horizontal dashed lines ($\Delta H = 22.5\,\mathrm{m}$).

β using Eq. (12), which will be necessary to calculate the amplitude modulation in Sec. III. This means that the point source approximation is only used to account for propagation effects in the present study.

III. RESULTS USING BOTH EXTENDED SOURCE MODELS

A. Configurations studied

In this study, the same 2.3 MW wind turbine as in Tian and Cotté (2016) and Cotté (2018) is considered, with a diameter of 93 m, a hub height of 80 m and three blades of length 45 m. As justified in Tian and Cotté (2016), each blade is decomposed into $M = 8$ segments to respect the constraint on the aspect ratio $L_m/c_m \geq 3,\ m = 1, .., M$ mentioned in Sec. II A. The rotation of the blade is divided into $N_\beta = 30$ angular positions (resolution of 12^o). The

214 wind velocity at at the hub height $z = 80\,\mathrm{m}$ is assumed to be $8\,\mathrm{m/s}$, and the angular velocity
215 of the rotor is $13\,\mathrm{rpm}$.

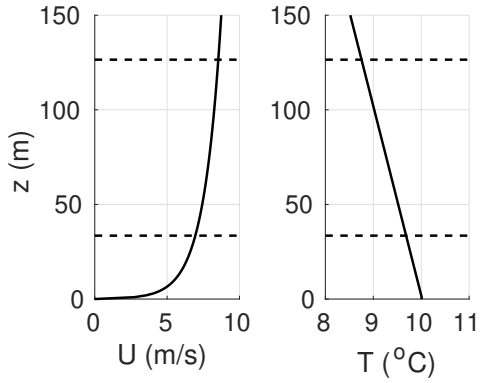

FIG. 4. Vertical profiles of wind speed $U(z)$ and temperature $T(z)$ in a neutral atmosphere. The minimum and maximum rotor heights are represented as horizontal dashed lines.

Two test cases are considered to evaluate the accuracy of the Amiet-PE and MM models. In the first case, only trailing edge noise is included, and the wind speed profile is assumed to be constant in the source model (no wind shear). The propagation conditions are assumed to be homogeneous ($c(z) = c_0$), with a finite impedance ground. The absence of refraction effects makes it possible to compare the results of the coupled model with the analytical solution in a homogeneous atmosphere based on Equations (12) and (13). In the second test-case, both trailing edge and turbulent inflow noise sources are considered, and the atmosphere is supposed to be neutral. Using the Monin-Obukhov similarity theory, this means that the vertical profiles of the mean wind speed $U(z)$ and of the temperature $T(z)$

are given by (Salomons, 2001):

$$U(z) = \frac{u_*}{\kappa} \ln\left(\frac{z}{z_0}\right), \tag{16}$$

$$T(z) = T_0 + \alpha_0 z, \tag{17}$$

where $u_* = 0.49\,\mathrm{m/s}$ is the friction velocity, $z_0 = 0.1\,\mathrm{m}$ is the surface roughness length, $T_0 = 10^o\mathrm{C}$ is the ground temperature, $\alpha_0 = -0.01\,\mathrm{K/m}$ is the dry adiabatic lapse rate, and $\kappa = 0.41$ is the von Kármán constant. The value of the friction velocity is chosen so that $U(z = 80\,\mathrm{m}) = 8\,\mathrm{m/s}$. The vertical profiles of $U(z)$ and $T(z)$ are plotted in Fig. 4. In both test-cases, the scattering effect of turbulence is not included in the model, which means that the SPL might be underestimated when a shadow zone is present (Cotté, 2018, Section 4.4).

The propagation domain has a size of 1200 m along x and 300 m along z. PE calculations are performed for 49 frequencies in order to predict the third octave band spectra between 100 Hz and 2000 Hz (Cotté, 2018). The ground impedance is calculated with a two-parameter variable porosity model, which is physically admissible and yields a better agreement with measurements than commonly used one-parameter models (e.g. Delany-Bazley or Miki), as shown by Dragna *et al.* (2015). The effective resistivity is $\sigma_e = 50\,\mathrm{kNs/m^4}$ and the rate of change of the porosity is $\alpha_e = 100\,\mathrm{m^{-1}}$, that are typical values for a natural soil (Dragna *et al.*, 2015, Table III).

In the Amiet-PE model, the initial starter is computed at a distance $x_{is} = 100\,\mathrm{m}$, and the far-field receiver is placed at $x_R = 1000\,\mathrm{m}$; see Fig. 2(b). In the MM model, the number of source heights N_h varies between 3 and 19, which corresponds to a height step ΔH decreasing from 45 m down to 5 m, considering $H_{\min} = 35\,\mathrm{m}$ and $H_{\max} = 125\,\mathrm{m}$. To give an

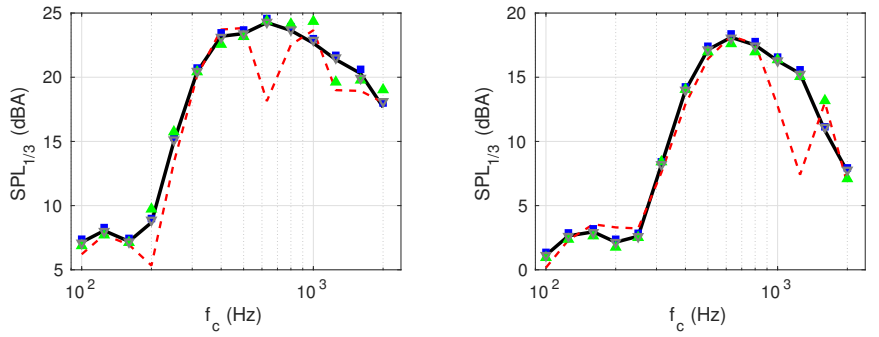

(a) (b)

FIG. 9. Third octave band spectrum of the SPL downwind ($\tau = 0^o$) at $z = 2\,\mathrm{m}$ and (a) $x = 500\,\mathrm{m}$ or (b) $x = 1000\,\mathrm{m}$: analytical solution (—), point source approximation (--), Amiet-PE (■), MM with 3 heights (▲) or 7 heights (▽). Color online.

order of magnitude of the computation time, a set of PE calculations for the 49 frequencies takes approximately 8 minutes to run on one core of a PC equipped with an Intel Xeon X5650 processor at 2.66 GHz. For each direction τ, the computation time of the MM model is thus between approximately 24 minutes with $N_h = 3$ and 2h30' with $N_h = 19$, and the computation time of the Amiet-PE model is greater than 30 hours.

B. Validation in a homogeneous atmosphere

First, the third octave band spectra of SPL averaged over one rotation are plotted in Fig. 5 for a receiver at a height of 2 m and at a distance of 500 m or 1000 m downwind ($\tau = 0^o$). The results with the point source approximation, the Amiet-PE model, and the MM model with three and seven source heights are compared to the analytical solution. Using the point source approximation, there are fluctuations due to ground interference dips that are much reduced using an extended source model. These fluctuations are still visible in the MM model with 3 source heights. Excellent agreement is found with the analytical solution using either the Amiet-PE model or the MM model with 7 source heights.

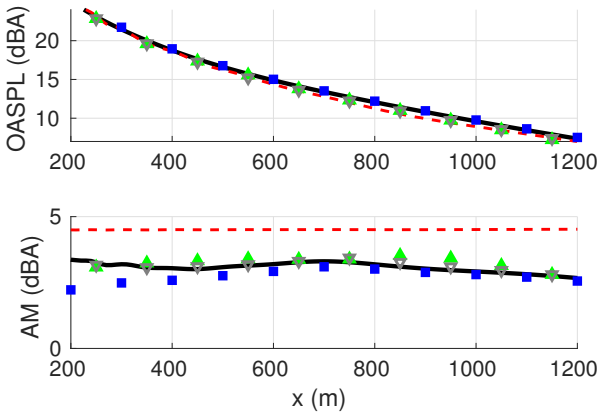

FIG. 6. OASPL and AM versus x at $z = 2\,\mathrm{m}$ crosswind ($\tau = 90^o$): analytical solution (—), point source approximation (- -), Amiet-PE (■), MM with 3 heights (▲) or 7 heights (▽). Color online.

Then, the overall sound pressure level (OASPL) averaged over one rotation and the amplitude modulation (AM) are plotted as a function of x in Fig. 6 for a receiver at a height of 2 m crosswind ($\tau = 90^o$). The amplitude modulation is defined as the difference between the maximum and the minimum of the OASPL over one rotation. On the one hand, all the OASPL predictions are within 1 dB(A) from the analytical calculation, even with the point source approximation. On the other hand, AM is seen to be much more sensitive to the source model used. As explained in Sec. II D, the point source approximation is only used to account for propagation effects in the present study, so it is theoretically possible to calculate AM using this source model, although the predicted value does not agree with the analytical solution. Using the Amiet-PE model, the AM predictions are accurate only for distances larger than 500 m approximately, which can be attributed to the fact that receivers at short ranges are far from the point at $x_R = 1000\,\mathrm{m}$ where all the propagation planes cross,

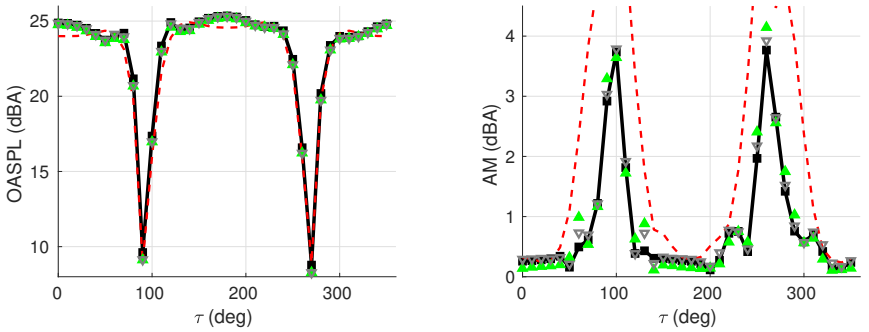

(a) (b)

FIG. 7. Directivity of (a) OASPL and (b) AM at $x = 1000\,\mathrm{m}$ and $z = 2\,\mathrm{m}$: analytical solution (—), point source approximation (- -), MM with 3 heights (▲) or 7 heights (▽). Color online.

as schematically shown in Fig. 2(b). The MM model yields very accurate AM values when at least 7 source heights are considered.

Finally, the directivities of OASPL and AM at a distance 1000 m and a height of 2 m are plotted in Fig. 7, using an angular step $\Delta\tau = 10^o$. The Amiet-PE calculations are not shown because it would be too computationally expensive with such a small value of $\Delta\tau$. In the OASPL directivity plot, some differences compared to the analytical solution are obtained with the point source approximation, that remain smaller than 1 dB(A) except close to the interference dips, while very accurate results are obtained using the MM model with 7 heights. The AM predictions using the point source approximation are completely off, while the ones obtained with the MM model are quite accurate, especially with 7 heights. The MM model predictions with 10 and 19 heights are not shown are they are almost identical to the predictions with 7 heights.

C. Results in a neutrally stratified atmosphere

In a neutral atmosphere, wind turbine noise propagation is completely different downwind and upwind, due to the presence of a shadow zone in the latter case. This is clearly seen

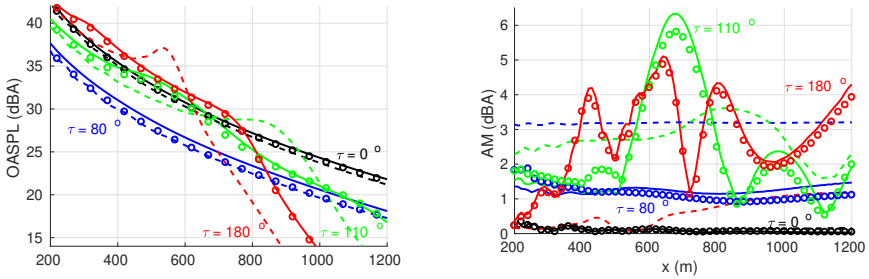

(a) (b)

FIG. 8. OASPL and AM with respect to x at $z = 2\,\mathrm{m}$ in a neutral atmosphere at $\tau = 0^o$ (downwind), $\tau = 80^o$, $\tau = 110^o$, and $\tau = 180^o$ (upwind): Amiet-PE (−), point source approximation (- -), MM with 19 heights (∘). Color online.

in the top plot of Fig. 8(a), where the evolution of OASPL with distance is plotted for propagation directions downwind, crosswind and upwind. Instead of considering the exact crosswind direction ($\tau = 90^o$), where the OASPL is very low, as seen in Fig. 7, two directions close to crosswind have been chosen: $\tau = 80^o$ and $\tau = 110^o$. For distances greater than approximately 800 m, the models predict a rapid decrease of the OASPL upwind, due to the shadow zone effect. This decrease is also seen for $\tau = 110^o$ although it is more gentle. Note that the shadow zone effect might be less pronounced in a real atmosphere, since the scattering effect due to turbulence has not been included in the present model, as discussed in Cotté (2018). In the directions $\tau = 0^o$ and $\tau = 80^o$, almost identical OASPL predictions are obtained using the Amiet-PE model, the MM model with 19 source heights and the point source approximation. In the directions $\tau = 110^o$ and $\tau = 180^o$, on the other hand, the point source approximation yields large errors at long distances. In the upwind direction, for instance, the shadow zone starts approximately 200 m earlier compared to the extended source model calculations.

To quantify the error made using various methods, let us define the maximum difference over a quantity $A(x)$ as:

$$\text{MaxDiff}(A) = \max_{500\,m \leq x \leq 1200\,m} |A(x) - A_{\text{ref}}(x)|\,, \tag{18}$$

where A_{ref} is a reference calculation. In Table I, the maximum difference MaxDiff(OASPL) is given using various models considering the Amiet-PE model as a reference. Note that the maximum difference is only calculated between 500 m and 1200 m in Eq. (18) as the validity of the Amiet-PE model is questionable at short ranges, as discussed in Sec. III B, and because the dwellings are generally located at least 500 m from the closest wind turbine. Table I shows that the point source approximation yields maximum differences greater than 1.0 dB in the crosswind and upwind directions. The MM model yields accurate results in all directions if at least 10 source heights are considered.

The evolution of AM with distance is plotted in Fig. 8(b) for the same four directions. The AM remains smaller than 0.2 dB(A) downwind, with similar results for all models. In the other directions, the AM is much higher, and is not well predicted using the point source approximation. The high values of the AM in upward-refracting conditions ($\tau = 110^o$ and $\tau = 180^o$) for distances greater than 400 m are attributed to the fact that the receiver will enter and leave the illuminated region during the blade rotation when it is close to the limit of the shadow zone, as shown in Barlas *et al.* (2017) and Cotté (2018). Since the shadow zone starts at a shorter range for higher frequency, the highest AM is encountered at different frequencies depending on the receiver positions (Cotté, 2018). In Table II, the maximum difference MaxDiff(AM) is given using the Amiet-PE model as a reference. It can be seen

TABLE I. Maximum difference MaxDiff(OASPL) with respect to the Amiet-PE model using the point source (PS) approximation and the MM model with 3 heights (MM3), 7 heights (MM7), 10 heights (MM10) and 19 heights (MM19) for different angles of propagation τ. Boldface values correspond to differences strictly greater than 1.0 dB.

τ	PS	MM3	MM7	MM10	MM19
0^o	0.6 dB	0.4 dB	0.3 dB	0.3 dB	0.3 dB
80^o	**1.1 dB**	1.0 dB	0.9 dB	0.8 dB	0.9 dB
110^o	**5.6 dB**	**3.6 dB**	**1.2 dB**	0.8 dB	0.8 dB
180^o	**11.0 dB**	**2.6 dB**	0.4 dB	0.4 dB	0.3 dB

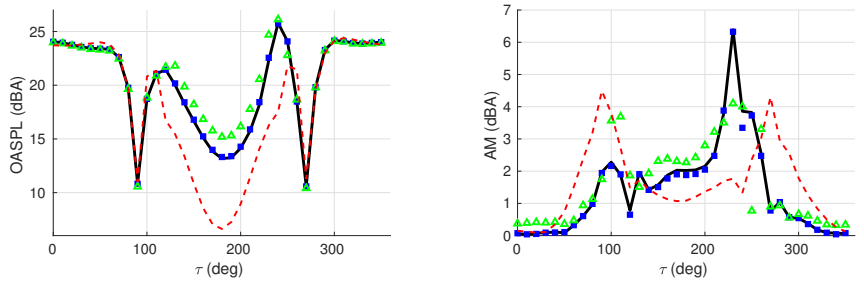

(a) (b)

FIG. 9. Directivity of (a) OASPL and (b) AM at $x = 1000$ m and $z = 2$ m in a neutral atmosphere: MM with 19 heights (—), MM with 10 heights (■), MM with 3 heights (△), and point source approximation (--). Color online.

that at least 10 source heights are needed in the MM model in order to obtain a maximum difference smaller than 1.1 dB in all directions.

To confirm that the MM model predictions converge with increasing source heights in all propagation directions, the directivities of OASPL and AM are plotted in Fig. 9 at a distance of 1000 m and a height of 2 m. Using the MM model with 19 source heights as the reference calculation, the difference between the OASPL predictions are observed in the

TABLE II. Maximum difference MaxDiff(AM) with respect to the Amiet-PE model using the point source (PS) approximation and the MM model with 3 heights (MM3), 7 heights (MM7), 10 heights (MM10) and 19 heights (MM19) for different angles of propagation τ. Boldface values correspond to differences strictly greater than 1.0 dB.

τ	PS	MM3	MM7	MM10	MM19
0^o	0.1 dB	0.4 dB	0.1 dB	0.0 dB	0.0 dB
80^o	**2.1 dB**	0.2 dB	0.3 dB	0.3 dB	0.4 dB
110^o	**3.4 dB**	**4.0 dB**	**1.3 dB**	**1.1 dB**	0.5 dB
180^o	**4.7 dB**	**3.8 dB**	**1.4 dB**	1.0 dB	0.4 dB

upwind directions ($100^o \leq \tau \leq 260^o$), with differences up to 8.3 dB(A) for the point source approximation, 2.4 dB(A) for the MM model with 3 heights, and only 0.3 dB(A) for the MM model with 10 heights. The same behavior is observed in the AM directivities, with differences up to 4.6 dB(A) for the point source approximation, 3.1 dB(A) for the MM model with 3 heights, and only 0.5 dB(A) for the MM model with 10 heights.

The movie Mm. 1 shows how the OASPL and AM horizontal directivities vary for distances between 200 m and 1200 m every 10 m. The relative contributions of trailing edge noise and turbulent inflow noise are also plotted, as can be seen in Fig. 10 where two snapshots of the movie corresponding to $x = 300$ m and $x = 1000$ m are shown. Up to 300 m approximately, refraction effects are small and the OASPL horizontal directivity keeps a dipole shape, as classically measured and predicted at short range (Buck *et al.*, 2016; Oer-

lemans and Schepers, 2009; Zhu *et al.*, 2005). At longer ranges, the OASPL directivity changes to an asymmetric shape, with small levels upwind, as seen for instance in Barlas *et al.* (2017) and McBride and Burdisso (2017). The AM directivity shows some peaks in various upwind directions depending on the propagation distance for $x > 400\,\mathrm{m}$. This can be attributed to the influence of the acoustic shadow zone, as explained previously. Note that significant AM values have also been reported in the downwind directions in other studies. For instance, Barlas *et al.* (2017) have obtained high AM values due to the effect of the wind turbine wake on acoustic propagation. This effect is not included in the present calculations.

Mm. 1. Directivity of OASPL and AM calculated with the MM model using $N_h = 10$ source heights with respect to distances between $x = 200\,\mathrm{m}$ and $x = 1200\,\mathrm{m}$ at $z = 2\,\mathrm{m}$ in a neutral atmosphere. The trailing edge noise (noted TEN) is shown in red, the turbulent inflow noise (noted TIN) is shown in blue, and the total prediction (noted Total) is shown in black. The wind is blowing from the left. File of type "avi" (8.4 MB)

It is also interesting to note in movie Mm. 1 that the OASPL directivities for trailing edge noise and turbulent inflow noise become quite different at large distances. This can be observed in the third octave band spectra of Fig. 11 at a distance of 1000 m in the downwind direction ($\tau = 0^o$), in the direction where turbulent inflow noise is dominant ($\tau = 120^o$), and in the direction where trailing edge noise is dominant ($\tau = 240^o$). At $\tau = 0^o$, the balance between the two noise generation mechanisms is similar to the one seen in the sound power level spectra, with trailing edge noise being dominant at high frequencies ($f > 250\,\mathrm{Hz}$) and turbulent inflow noise being dominant at low frequencies ($f < 250\,\mathrm{Hz}$). On the other hand,

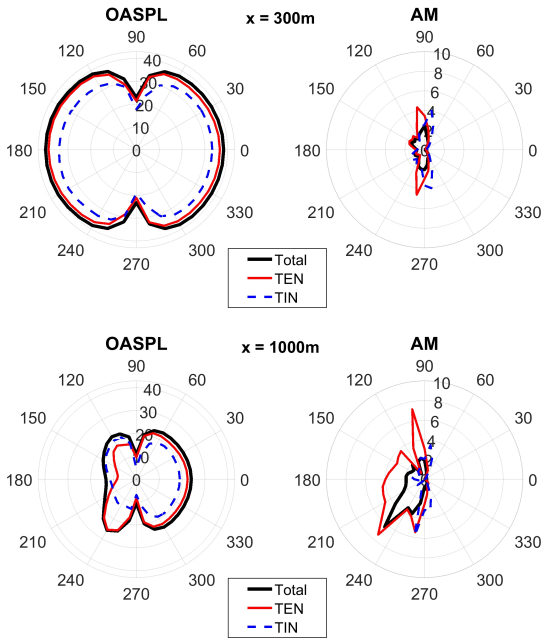

FIG. 10. Directivity of OASPL and AM calculated with the MM model using $N_h = 10$ source heights at $z = 2\,\mathrm{m}$ and $x = 300\,\mathrm{m}$ (top) or $x = 1000\,\mathrm{m}$ (bottom) in a neutral atmosphere. The thick solid line corresponds to the total prediction (noted Total), the thin solid line to the trailing edge noise (noted TEN), and the thin dashed line to turbulent inflow noise (noted TIN). The wind is blowing from the left.

turblent inflow noise becomes dominant for most frequencies at $\tau = 120^o$, while trailing edge noise becomes dominant for most frequencies at $\tau = 240^o$.

IV. CONCLUSION

In this study, two methods have been tested to include extended aeroacoustic source models in a parabolic equation code for wind turbine noise propagation in an inhomogeneous atmosphere. These two methods have been compared to the point source approximation that

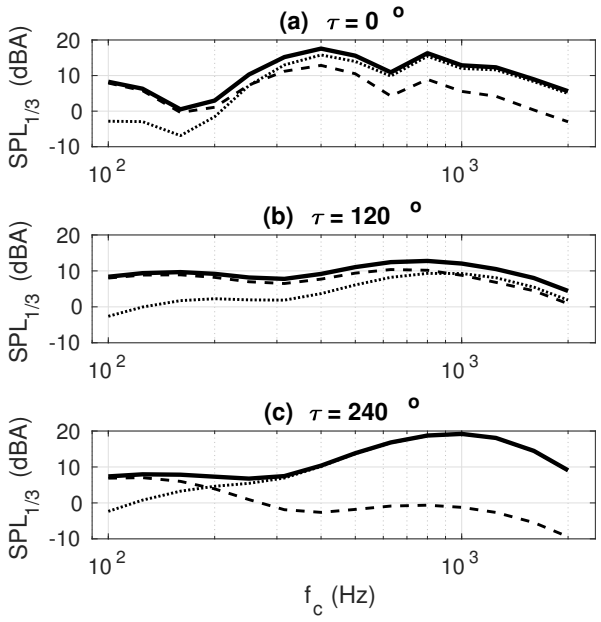

FIG. 11. Third octave band spectrum of the SPL in a neutral atmosphere at $x = 1000\,\mathrm{m}$ and $z = 2\,\mathrm{m}$ calculated with the MM model with 10 source heights at (a) $\tau = 0^o$, (b) $\tau = 120^o$, and (c) $\tau = 240^o$: total prediction (solid lines), trailing edge noise only (dotted lines), and turbulent inflow noise only (dashed lines).

is classically used in wind turbine noise propagation studies. The source model is based on Amiet's theory, and the parabolic equation code uses a split-step Padé approximant. In the first method, called Amiet-PE, an initial starter is obtained for each segment of the blade using the backpropagation approach. This method enables one to accurately model the directivity of the noise sources but is very computationally intensive. In the second method, the blade segments are viewed as moving monopole sources (MM model), and only a limited number of parabolic equation simulations are needed depending on the number of source heights considered to discretize the rotor plane.

The various models are first validated using an analytical reference solution in a homogeneous medium. The Amiet-PE model and the MM model with at least 7 source heights ($\Delta H \leq 15\,\mathrm{m}$) are in excellent agreement with the reference solution, in terms of spectra, OASPL and AM. The point source approximation is relatively accurate to predict the OASPL, but it is unable to predict the AM, and tends to exaggerate the ground interference dips in the spectra, even at large distances from the source.

The models are then compared in a neutrally stratified atmosphere, characterized by a logarithmic velocity profile. The most challenging propagation conditions are encountered upwind, where an acoustic shadow zone appears for propagation distances greater than approximately 400 m. The point source approximation fails to calculate the correct OASPL in these directions, because it predicts a shadow zone that starts too close to the wind turbine. In order to correctly capture the AM behavior upwind, the Amiet-PE model and the MM model with at least 10 source heights ($\Delta H \leq 10\,\mathrm{m}$) are shown to yield accurate results. The MM model is much more computationally effective than the Amiet-PE model, with a ratio $MN_\beta/N_h \approx 24$ between the two models with $N_h = 10$ source heights.

The MM model proposed in this article could be used in the future to study the effect of strong wind speed gradients, that is potentially the source of amplitude modulation at night (van den Berg, 2008; Zajamsek *et al.*, 2016), the influence of the wind turbine wake on propagation (Barlas *et al.*, 2017), or the combined influence of topography and meteorology, using for instance the rotated PE approach described in Lihoreau *et al.* (2006).

ACKNOWLEDGMENTS

The author would like to thank Benoit Gauvreau and David Ecotière from the Environmental Acoustics Unit (UMRAE), and Tommy Rigall from IMSIA for their useful comments on the manuscript.

Barlas, E., Zhu, W., Shen, W., Dag, K., and Moriarty, P. (**2017**). "Consistent modelling of wind turbine noise propagation from source to receiver," Journal of the Acoustical Society of America **142**(5), 3297–3310.

Buck, S., Oerlemans, S., and Palo, S. (**2016**). "Experimental characterization of turbulent inflow noise on a full-scale wind turbine," Journal of Sound and Vibration **385**, 219–238.

Christophe, J., Anthoine, J., and Moreau, S. (**2009**). "Amiet's Theory in Spanwise-Varying Flow Conditions," AIAA Journal **47**(3), 788–790.

Collins, M. (**1993**). "A split-step Padé solution for the parabolic equation method," Journal of the Acoustical Society of America **93**(4), 1736–1742.

Cotté, B. (**2018**). "Coupling of an aeroacoustic model and a parabolic equation code for long range wind turbine noise propagation," Journal of Sound and Vibration **422**, 343–357.

Dallois, L., Blanc-Benon, P., and Juvé, D. (**2002**). "The modelling of long range sound propagation: recent developments in the PE method," in *Tenth International Symposium on Long-Range Sound Propagation*.

Dragna, D., Attenborough, K., and Blanc-Benon, P. (**2015**). "On the inadvisability of using single parameter impedance models for representing the acoustical properties of ground surfaces," Journal of the Acoustical Society of America **138**(4), 2399–2413.

Galindo, M. (**1996**). "Approximations in the PE method. Phase and level errors in a downward refracting atmosphere," in *Seventh International Symposium on Long-Range Sound Propagation, Lyon, France*.

Gilbert, K.E., and White, M.J. (**1989**). "Application of the parabolic equation to sound propagation in a refracting atmosphere," Journal of the Acoustical Society of America **85**(2), 630–637.

Heimann, D., Englberger, A., and Schady, A. (**2018**). "Sound propagation through the wake flow of a hilltop wind turbine – a numerical study," Wind Energy **21**, 650–662.

Larsson, C., and Öhlund, O. (**2014**). "Amplitude modulation of sound from wind turbines under various meteorological conditions," Journal of the Acoustical Society of America **135**(1), 67–73.

Lee, S., Lee, D., and Honhoff, S. (**2016**). "Prediction of far-field wind turbine noise propagation with parabolic equation," Journal of the Acoustical Society of America **140**(2), 767–778.

Lihoreau, B., Gauvreau, B., Bérengier, M., Blanc-Benon, P., and Calmet, I. (**2006**). "Outdoor sound propagation modeling in realistic environments: Application of coupled parabolic and atmospheric models," Journal of the Acoustical Society of America **120**(1), 110–119.

McBride, S., and Burdisso, R. (**2017**). "A comprehensive hamiltonian ray tracing technique for wind turbine noise propagation under arbitrary weather conditions," in *Seventh International Meeting on Wind Turbine Noise, Rotterdam, Netherlands*.

Oerlemans, S., and Schepers, J. G. (**2009**). "Prediction of wind turbine noise and validation against experiment," International Journal of Aeroacoustics **8**, 555–584.

Prospathopoulos, J., and Voutsinas, S. (**2007**). "Application of a ray theory model to the prediction of noise emissions from isolated wind turbines and wind parks," Wind Energy **10**, 103–119.

Roger, M., and Moreau, S. (**2010**). "Extensions and limitations of analytical airfoil broadband noise models," International Journal of Acoustics **9**(3), 273–305.

Rozenberg, Y., Roger, M., and Moreau, S. (**2010**). "Rotating Blade Trailing-Edge Noise: Experimental Validation of Analytical Model," AIAA Journal **48**(5), 951–962.

Salomons, E. M. (**2001**). *Computational Atmospheric Acoustics* (Kluwer Academic Publishers).

Sinayoko, S., Kingan, M., and Agarwal, A. (**2013**). "Trailing edge noise theory for rotating blades in uniform flow," Proc. R. Soc. A **469**, 20130065.

Tian, Y., and Cotté, B. (**2016**). "Wind turbine noise modeling based on Amiet's theory: Effects of wind shear and atmospheric turbulence," Acta Acustica united with Acustica **102**, 626–639.

van den Berg, G. (**2008**). "Wind turbine power and sound in relation to atmospheric stability," Wind Energy **11**, 151–169.

442 Zajamsek, B., Hansen, K., Doolan, C., and Hansen, C. (**2016**). "Characterisation of wind
443 farm infrasound and low-frequency noise," Journal of Sound and Vibration **370**, 176–190.
444 Zhu, W., Heilskov, N., Shen, W., and Sørensen, J. (**2005**). "Modeling of aerodynamically
445 generated noise from wind turbines," Journal of Solar Energy Engineering **127**, 517–528.